The JWST Weather Report from the Isolated Exoplanet Analog SIMP 0136+0933: Pressure-dependent Variability Driven by Multiple Mechanisms

Allison M. McCarthy[1] , Johanna M. Vos[2,3] , Philip S. Muirhead[1] , Beth A. Biller[4,5] , Caroline V. Morley[6] ,
Jacqueline Faherty[7] , Ben Burningham[8] , Emily Calamari[9,7] , Nicolas B. Cowan[10,11] , Kelle L. Cruz[12,9,7] ,
Eileen Gonzales[13] , Mary Anne Limbach[14] , Pengyu Liu[4,5,15] , Evert Nasedkin[2] , Genaro Suárez[7] , Xianyu Tan[16] ,
Cian O'Toole[2] , Channon Visscher[17,18] , Niall Whiteford[7] , and Yifan Zhou[19]

[1] Department of Astronomy & The Institute for Astrophysical Research, Boston University, 725 Commonwealth Avenue, Boston, MA 02215, USA; alliemc@bu.edu
[2] School of Physics, Trinity College Dublin, The University of Dublin, Dublin 2, Ireland
[3] Department of Astrophysics, American Museum of Natural History, Central Park West at 79th Street, New York, NY 10034, USA
[4] Institute for Astronomy, University of Edinburgh, Royal Observatory, Edinburgh EH9 3HJ, UK
[5] Centre for Exoplanet Science, University of Edinburgh, Edinburgh, UK
[6] Department of Astronomy, University of Texas at Austin, Austin, TX 78712, USA
[7] Department of Astrophysics, American Museum of Natural History, New York, NY 10024, USA
[8] Centre for Astrophysics Research, School of Physics, Astronomy and Mathematics, University of Hertfordshire, Hatfield AL10 9AB, UK
[9] Graduate Center of the City University of New York, New York, NY 10016, USA
[10] Department of Earth & Planetary Sciences, McGill University, 3450 rue University, Montréal, QC H3A 0E8, Canada
[11] Department of Physics, McGill University, Montréal, QC H3A 2T8, Canada
[12] Department of Physics and Astronomy, Hunter College, City University of New York, 365 Fifth Avenue, New York, NY 10016, USA
[13] Department of Physics and Astronomy, San Francisco State University, 1600 Holloway Avenue, San Francisco, CA 94132, USA
[14] Department of Astronomy, University of Michigan, Ann Arbor, MI 48109, USA
[15] Leiden Observatory, Leiden University, PO Box 9513, 2300 RA Leiden, The Netherlands
[16] Tsung-Dao Lee Institute & School of Physics and Astronomy, Shanghai Jiao Tong University, Shanghai 201210, People's Republic of China
[17] Chemistry & Planetary Sciences, Dordt University, Sioux Center IA 51250, USA
[18] Center for Extrasolar Planetary Systems, Space Science Institute, Boulder, CO 80301, USA
[19] Department of Astronomy, University of Virginia, 530 McCormick Road, Charlottesville, VA 22904, USA

Abstract

Isolated planetary-mass objects share their mass range with planets but do not orbit a star. They lack the necessary mass to support fusion in their cores and thermally radiate their heat from formation as they cool, primarily at infrared wavelengths. Many isolated planetary-mass objects show variations in their infrared brightness consistent with nonuniform atmospheric features modulated by their rotation. SIMP J013656.5+093347.3 is a rapidly rotating isolated planetary-mass object, and previous infrared monitoring suggests complex atmospheric features rotating in and out of view. The physical nature of these features is not well understood, with clouds, temperature variations, thermochemical instabilities, and infrared-emitting aurora all proposed as contributing mechanisms. Here we report JWST time-resolved low-resolution spectroscopy from 0.8 to 11 μm of SIMP J013656.5 +093347.3, which supports the presence of three specific features in the atmosphere: clouds, hot spots, and changing carbon chemistry. We show that no single mechanism can explain the variations in the time-resolved spectra. When combined with previous studies of this object indicating patchy clouds and aurorae, these measurements reveal the rich complexity of the atmosphere of SIMP J013656.5+093347.3. Gas giant planets in the solar system, specifically Jupiter and Saturn, also have multiple cloud layers and high-altitude hot spots, suggesting these phenomena are also present in worlds both within and beyond our solar system.

Unified Astronomy Thesaurus concepts: Brown dwarfs (185); T dwarfs (1679); Stellar atmospheres (1584);
Exoplanet atmospheres (487); Exoplanet atmospheric variability (2020); Exoplanet atmospheric structure (2310)

1. Introduction

Since its first observations in 2022, JWST has been transforming our understanding of extrasolar atmospheres. JWST's superb resolution and sensitivity are allowing detailed spectroscopic study across wavelengths previously only accessible with photometry or low-resolution spectroscopy. As such, JWST is revealing new insights into condensation and isotopic abundances (H. Kühnle et al. 2024), disequilibrium chemistry (S. A. Beiler et al. 2024), and possible auroral heating (J. K. Faherty et al. 2024) in the faintest substellar objects. As well as allowing access to very faint atmospheres, the spectacular sensitivity of JWST allows high-signal-to-noise-ratio (SNR) broad coverage spectra to be obtained with integrations short enough to allow detailed time-series analysis, including wavelength regions that are essentially inaccessible from the ground. These findings are reshaping our understanding of the formation, evolution, and structure of extrasolar atmospheres. Isolated planetary-mass objects, with their similar temperature, gravity, and chemistry to exoplanets, serve as analogs for directly imaged exoplanets (J. K. Faherty et al. 2016). However, without the light of a host star, these isolated objects are easier to observe, making them ideal laboratories for studying atmospheric properties.

Photometric monitoring in the optical, near-infrared (near-IR), and mid-infrared (mid-IR) has uncovered dramatic

variability that is common among brown dwarfs and isolated planetary-mass objects (e.g., J. Radigan 2014; S. A. Metchev et al. 2015; J. M. Vos et al. 2022). Inhomogeneous cloud cover (J. Radigan 2014), thermochemical instabilities (P. Tremblin et al. 2016), hot spots (T. D. Robinson & M. S. Marley 2014a), and auroral activity (G. Hallinan et al. 2015) have all been suggested as drivers of this variability. These variability patterns have been linked to dynamical processes, such as cloud radiative feedback (X. Tan & A. P. Showman 2021) and convective perturbations (X. Zhang & A. P. Showman 2014).

Multiwavelength observations are crucial for probing different atmospheric layers and providing a comprehensive view of vertical structure (E. Buenzli et al. 2012; D. Apai et al. 2013). With JWST, we now have the capability for spectroscopic monitoring across an unprecedented wavelength range, essential for investigating atmospheric structures and processes in brown dwarfs, isolated planetary-mass objects, and directly imaged exoplanets. JWST's NIRSpec covers 0.6–5 μm (P. Jakobsen et al. 2022), ideal for observing the brightest emission from these objects. JWST's MIRI extends this to 28 μm, allowing exploration of the variability of mid-IR silicate absorption features for the first time (G. Suárez & S. Metchev 2022).

Recently, B. A. Biller et al. (2024) presented the first JWST spectroscopic monitoring of the brown dwarf binary WISE J104915.57-531906.1AB (WISE1049AB), detecting significant variability across 1–11 μm. The wavelength-dependent light-curve shapes were attributed to different pressure layers in the atmosphere, showcasing JWST's ability to probe atmospheric structure in detail.

Here, we present the first JWST spectroscopic monitoring campaign of an isolated planetary-mass object: SIMP J013656.5+093347.3 (SIMP 0136+0933). As the brightest isolated planetary-mass object, it has been studied extensively with ground-based and space-based programs (e.g., É. Artigau et al. 2006; 2009; D. Apai et al. 2013; H. Yang et al. 2016; A. M. McCarthy et al. 2024). With an effective temperature of ~1100 K (T2.5), it lies in the L/T transition region, known for high-amplitude variability driven by silicate cloud breakup (J. Radigan 2014; P. Liu et al. 2024). SIMP 0136+0933 has shown variability amplitudes up to 5% in the J band (É. Artigau et al. 2009) and a rotation period of ~2.4 hr (B. Croll et al. 2016; H. Yang et al. 2016). Its near-IR variability has been linked to patchy clouds (D. Apai et al. 2013; A. M. McCarthy et al. 2024), while mid-IR variability may be driven by CO/CH$_4$ fingering convection (P. Tremblin et al. 2020). Strong pulsed radio emission on SIMP 0136+0933 indicates auroral activity (M. M. Kao et al. 2016, 2018).

In this Letter, we present JWST observations of SIMP 0136 +0933 (Section 2). We describe our reduced spectra and light curves in Section 3. Section 4 outlines our analysis, including light-curve clustering and model interpretation. Finally, in Section 5, we summarize our findings and suggest directions for future work on brown dwarfs and planetary-mass objects.

2. Observations and Data Reduction

As part of the JWST Cycle 2 program GO 3548 (PI: Vos), we observed just over one full rotation period of SIMP 0136+0933 sequentially with NIRSpec followed by MIRI. The NIRSpec and MIRI observations were carried out in an noninterruptible sequence since SIMP 0136+0933 is known to evolve significantly over the course of a few rotations (É. Artigau et al. 2009). This observing strategy ensured that we captured

SIMP 0136+0933 in a similar atmospheric state across both instruments. NIRSpec Bright Object Time Series (BOTS) observations were carried out from UT 18:40:56 to 22:05:06 on 2023 July 23. MIRI Low Resolution Spectroscopy (LRS) Time Series Observations (TSOs) were then carried out from UT 22:05:11 on 2023 July 23 to UT 01:38:38 on 2023 July 24, with a brief background observation from UT 01:38:42 to UT 02:03:16 on 2023 July 24.

We used the PRISM/CLEAR mode for our NIRSpec/BOTS observations to obtain low-resolution time-series spectroscopy from 0.6 to 5.3 μm with a resolution of $R = 30$–300. WATA target acquisition was carried out with the F110W filter and the NRSRAPID readout pattern with three groups. For science observations, we used the SUB512 subarray and seven groups per integration, yielding a cadence of 1.8 s to avoid saturation, obtaining a total of 5726 integrations.

MIRI TSOs were obtained immediately after the NIRSpec/BOTS observations. We used the LRS slitless mode, the P750L disperser, and FAST readout mode to provide maximal samples up the ramp, yielding time-resolved spectra at 5–14 μm with a resolution of $R = 40$–160. We used the F560W filter and the FASTR1 readout patterns with five groups per integration for target acquisition. For the science observations we then obtained a total of 575 integrations using the LRS SLITLE-SSPRISM subarray, FASTR1 readout, and 120 groups per integration, yielding a cadence of 19.2 s.

2.1. NIRSpec Data Reduction

The NIRSpec/BOTS data were reduced using the JWST STScI pipeline version 1.14.0, Calibration Reference Data System (CRDS) Version 11.17.19 and CRDS context file `jwst_1253.pmap`. The JWST Pipeline Stage 1 was used with default settings to apply basic detector-level corrections to all exposures. Following advice from the JWST Helpdesk, 1/f noise originating from JWST detector readout electronics was removed before running Stage 2. JWST NIRSpec readout electronics generate significant 1/f noise during detector operations and signal digitization. This noise varies from column to column and appears as vertical banding that spans the entire width of the 2D spectral images in NIRSpec/BOTS observations, and it can introduce systematic errors and significant scatter in light curves. We removed the 1/f noise by subtracting the median background flux per column across the spectral image. JWST Pipeline Stage 2 is then used to extract the 1D spectrum using an extraction width of 3 pixels. We run Stage 2 twice to produce the two final data products, one that is optimized for absolute flux (Figure 1) and the other for relative light curves (Figure 2), for further analysis. To produce the final calibrated spectra for each image we run the Stage 2 pipeline using default parameters, which includes all steps. The final extracted near-IR spectra are of excellent quality, with a median SNR of 64 per 1.8 s exposure. To produce relative light curves for variability analysis, we skip the flat-field and photometric calibration steps, following advice from the JWST helpdesk and recent examples of high-precision exoplanet transit and eclipse light curves from the literature (Z. Rustamkulov & Transiting Exoplanet Community ERS Team 2022; E.-M. Ahrer et al. 2023; L. Alderson et al. 2023; D. K. Sing et al. 2024; L. Welbanks et al. 2024). Additionally, the curvature of the spectral trace is accounted for and 1/f noise is corrected in the relative light-
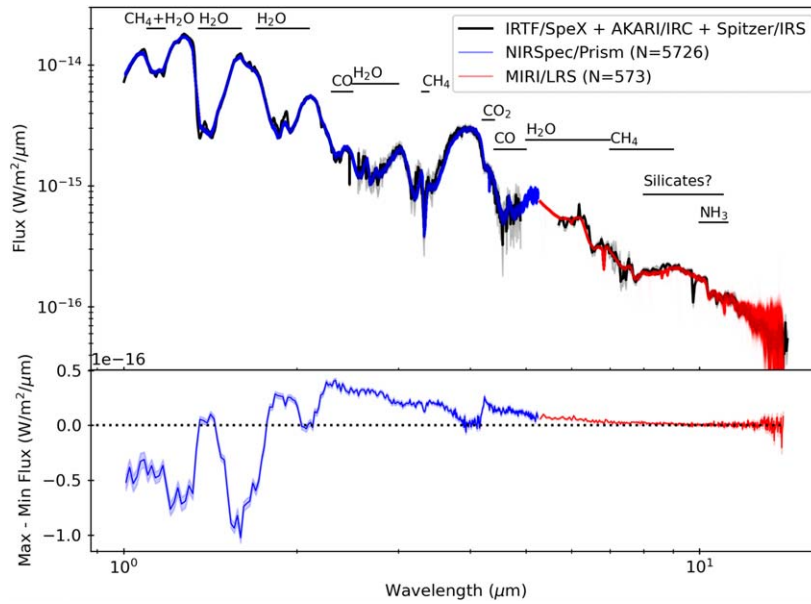
Figure 1. Top panel: final flux-calibrated NIRSpec/PRISM (blue) and MIRI/LRS (red) spectra of SIMP 0136+0933, compared to the spectrum presented in J. M. Vos et al. (2023; black) and error (shaded in gray). For the NIRSpec and MIRI spectra, each spectrum is plotted individually. Notable absorption features are indicated by horizontal black lines and their labels. For each instrument, we plot each spectrum individually, so the observed spread is a result of both noise and intrinsic variability. Bottom panel: minimum spectrum subtracted from the maximum spectrum. The maximum and minimum spectra were identified using the 4.5–5.1 μm light curve (Figure 4).

curve reduction, although this does not cause a significant difference in the light curves.

2.2. MIRI Data Reduction

The MIRI/LRS TSOs were reduced using the same pipeline version and context file as the NIRSpec/BOTS data. Stage 1 processing was applied via `calwebb_detector1` using default settings. The Stage 2 pipeline assigns world coordinate system coordinates, source type, flat-fielding, photometric calibration, and spectral extraction. The Stage 2 pipeline for TSOs does not include a background subtraction so we implement a custom background subtraction by defining a rectangular background region in the target image with the same width as the source extraction aperture and calculating the median value as a function of wavelength. The final extracted mid-IR spectra are of good quality, with a median SNR of 124 per 19.2 s exposure. The MIRI data is shown in Figure 1 (red) and Figure 3.

3. Results

3.1. Spectra

In Figure 1 we present the final, flux-calibrated NIRSpec/PRISM and MIRI/LRS spectra for each exposure for SIMP 0136+0933. For both instruments, we plot each spectrum individually, so the observed spread shown in the top panel of Figure 1 is a result of both noise and intrinsic variability. The bottom panel shows the difference between the "maximum" and "minimum" spectra, which is determined from the relative maximum and minimum of the 4.5–5.1 μm light curve shown in Figure 4.

The JWST spectra are remarkably consistent with the spectrum analyzed by J. M. Vos et al. (2023), which consists of three spectra (Infrared Telescope Facility/SpeX PRISM, AKARI/Infrared Camera, and Spitzer/Infrared Spectrograph, IRS) taken at different epochs. As expected for an early-T

dwarf, we see absorption features driven by molecules such as H_2O, CH_4, and CO. The silicate absorption feature at 8.0–11 μm is weak if present, which is consistent with its spectral type (G. Suárez & S. Metchev 2022). The spectrum within the silicate region aligns with the Spitzer/IRS spectrum analyzed by J. M. Vos et al. (2023). Beyond wavelengths of 11 μm, there is a noticeable drop in SNR that causes the increased spread beyond these wavelengths.

The bottom panel of Figure 1 highlights that every wavelength is variable. Additionally, the difference in the spectra demonstrates how each wavelength has unique temporal variations. If all wavelengths displayed the same overall variations, the difference between the "maximum" and "minimum" spectra would always be positive. Note that the "maximum" and "minimum" are selected from the 4.5–5.1 μm light curves shown in Figure 4. There is no global maximum or minimum, since the variability is extremely wavelength dependent. A detailed spectral analysis, which will empirically measure molecular abundances and characterize the vertical cloud structure, will be presented in a future paper. This Letter will focus on analysis of the relative light curves.

3.2. Light Curves

We present variability maps of the NIRSpec and MIRI observations in Figures 2 and 3. The variability map is a 2D representation of the normalized flux as a function of wavelength and time (refer to B. A. Biller et al. 2024 for more details). The NIRSpec variability map interpolates over wavelengths that had poor SNR or clear anomalous points. The MIRI map includes all wavelengths, and the drop in SNR past ~11 μm due to throughput is clearly visible. Additionally, both the NIRSpec and MIRI wavelength resolution increase toward redder wavelengths.

Figures 2 and 3 display binned light curves for both the NIRSpec and MIRI data. NIRSpec light curves are binned in 0.2 μm wavelength bins and by 1 minute in time. MIRI light
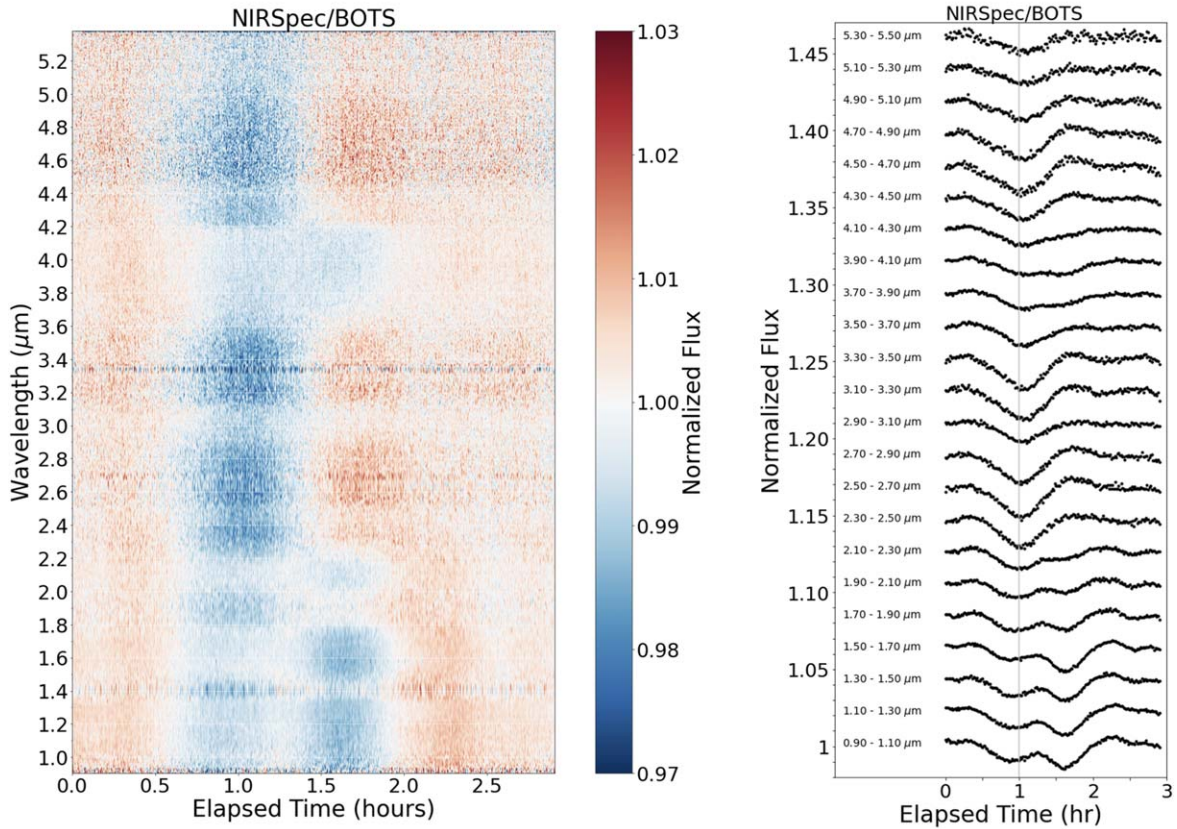
Figure 2. Left: variability map showing the reduced NIRSpec/BOTS spectroscopic relative light curves. The variability map is a 2D representation of the relative flux as a function of time and wavelength. Right: binned light curves for NIRSpec. The data are binned by 0.2 μm in wavelength and 1 minute in time. The gray vertical lines at 1 hr mark the approximate minimum of the light curves and denote the "start" of one full rotation (2.4 hr) of the object. The data used to create the variability map and light curves are available on the SIMPLE archive.

curves are binned by 0.5 μm in wavelength and by 1 minute in time. Prior to creating the binned light curves, we removed wavelengths whose light curves had an SNR $<$ 25 or displayed anomalous behavior.

Figures 2 and 3 highlight the complex nature of the observed light curves as a function of wavelength, pointing to a dynamic atmosphere. The NIRSpec light curves shown in Figure 2 are variable at all wavelengths and exhibit several distinct features. At bluer wavelengths, there is a distinct double trough feature, where the relative depths of the two troughs vary as a function of wavelength. Moving toward the redder wavelengths, the light-curve shape exhibits a single trough. From ~3.5 to 4.3 μm the light-curve shape changes again, before returning to one deep trough at the reddest of wavelengths.

For the MIRI data, there are also patterns in the data. Overall, MIRI displays a maximum deviation of variability, the difference between the maximum and minimum normalized flux values, which is less than the variability observed in NIRSpec. From ~4.2 to ~8.5 μm, there is a double-peaked feature, with the first peak at ~4.0 hr and the secondary peak at ~5.0 hr (also shown in Figure 4). At $\gtrsim$ 8.5 μm, the behavior changes to a smoother light-curve behavior with smaller maximum deviation.

NIRSpec and MIRI share a region of wavelength space that allows us to create a light curve that covers the full observation duration. We plot light curves spanning this 4.5–5.1 μm region in Figure 4. We identify a minimum and maximum within the NIRSpec and MIRI portion of the light curve by eye, which is shown by the solid green and dashed purple vertical lines in

Figure 4. We find that, at these wavelengths, the light curve does not change significantly from one rotation to the next (compare to B. A. Biller et al. 2024, who found evolution in light-curve structure from rotation to rotation). Spectroscopic observations spanning longer than two rotations will be necessary to probe in detail the long-term evolution of the atmosphere of SIMP 0136+0933.

4. Analysis and Discussion

4.1. Light-curve Modeling

We used celerite2 (D. Foreman-Mackey et al. 2017; D. Foreman-Mackey 2018) to fit a model to each of our NIRSpec and MIRI light curves, following the approach of A. M. McCarthy et al. (2024). The celerite2 software employs Gaussian processes to model data as correlated noise, with the degree of correlation set by a chosen kernel function (C. E. Rasmussen & C. K. I. Williams 2006). We used a combination of two SHOTerm kernels, which represent stochastically driven, damped simple harmonic oscillators with a fixed period matched to the measured rotational period of SIMP 0136+0933 (2.4 hr É. Artigau et al 2009; H. Yang et al. 2016). Together, the kernels have six free parameters, and we included one additional parameter to capture additional measurement uncertainty following a recommended approach in the celerite2 documentation. We then used the emcee Markov Chain Monte Carlo software package to explore the values of the free parameters that best describe the data (D. Foreman-Mackey et al. 2013a). The set of free parameters
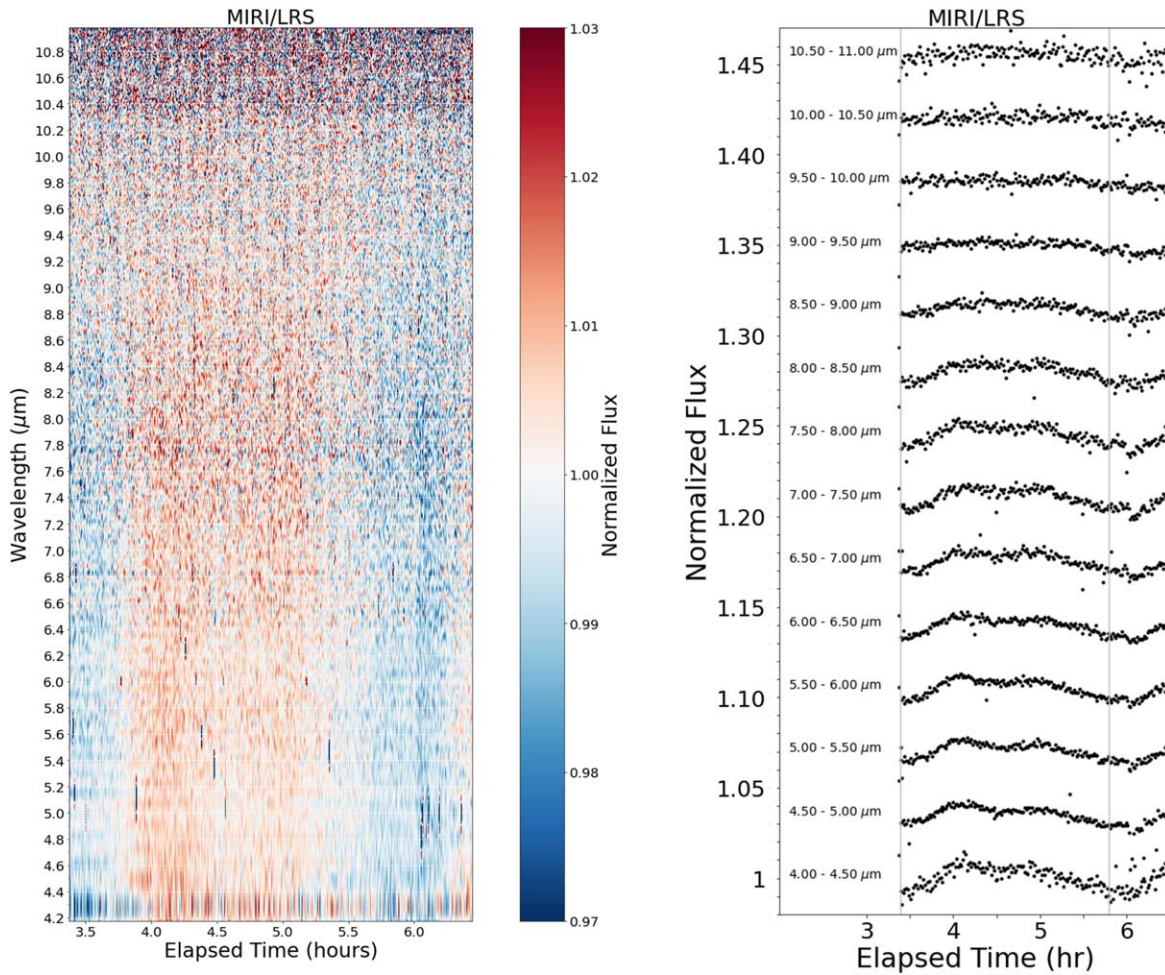
Figure 3. Left: variability map showing the reduced MIRI/LRS spectroscopic light curves. The variability map is a 2D representation of the relative flux as a function of time and wavelength. Right: binned light curves for MIRI. The data are binned by 0.5 μm in wavelength and 1 minute in time. The gray vertical lines at 3.4 and 5.8 hr represent one complete rotation (2.4 hr) of the object. The data used to create the variability map and light curves are available on the SIMPLE archive.
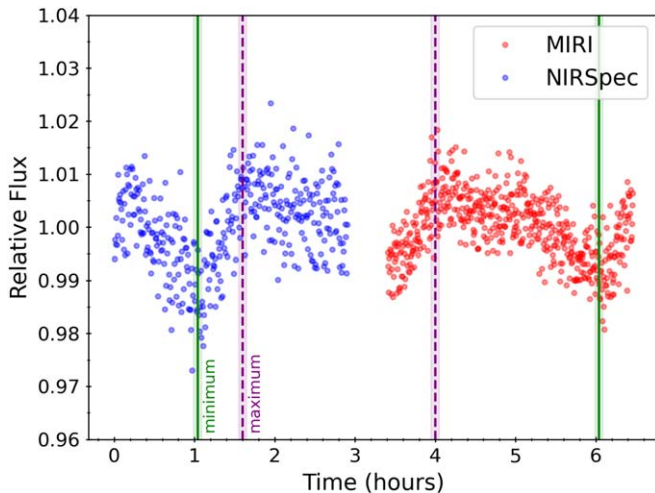
Figure 4. NIRSpec and MIRI light curves in the overlapping wavelength regions (4.5–5.1 μm). The binned NIRSpec light curve (27 s cadence) is shown in blue and the MIRI light curve (19 s cadence) is shown in red. Green solid lines and purple dashed lines indicate timestamps for the "maximum" and "minimum" spectra referenced in Figure 1.

with the highest posterior value was used to calculate the best-fitting model. When fitting the light curves, we did not bin the NIRSpec data in wavelength or time. We binned the MIRI light

curves by 0.5 μm to increase the signal to noise. The celerite2 fits are shown in gray in panel (a) of Figures 5 and 6.

4.2. Light-curve Clustering

The variability maps and light curves presented in Figures 2 and 3 show complex light-curve behavior. We observe variability across all wavelengths (also discussed in Section 4.4), with similar behaviors seen across distinct wavelength regions. Wavelengths with similar light curves are likely impacted by the same mechanism(s), so by grouping together similar-shaped light curves we can investigate these mechanism(s).

We use a *K*-means clustering algorithm from scikit-learn to efficiently group together light curves with similar features, capturing details difficult to discern visually, using the approach employed by B. A. Biller et al. (2024). We bin every 50 points from the celerite2 highest-likelihood fits, which results in a cadence of ~55 s for NIRSpec, which we feed to the *K*-means clustering algorithm. We do not bin the NIRSpec data in wavelength. For the MIRI data, since we have already binned the data in wavelength space, we do not bin it in time for the *K*-means clustering algorithm.

After making cuts where the average SNR < 25 and at wavelengths where there were clear anomalous points in the data, we have 362 wavelengths in NIRSpec, producing the
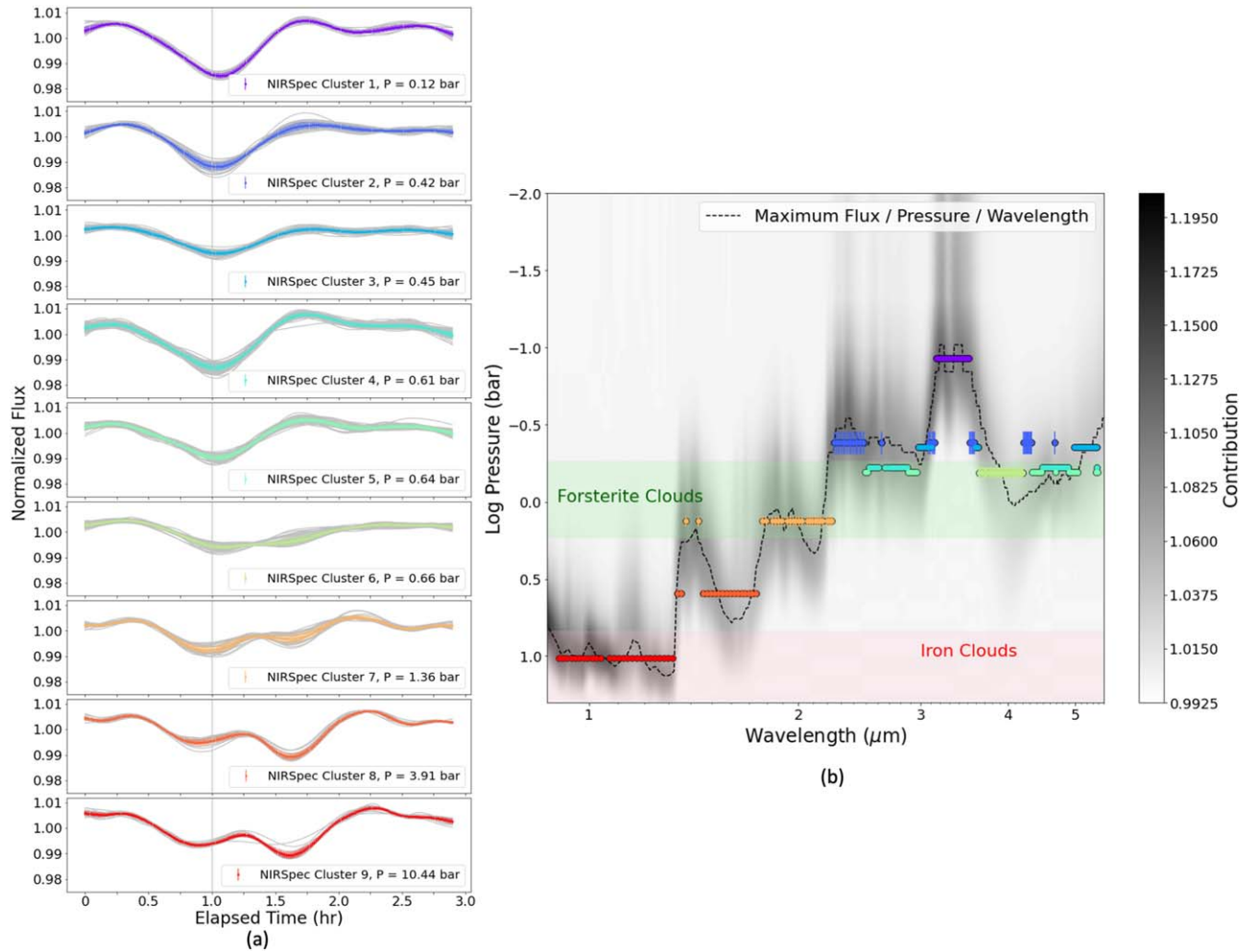
Figure 5. Panel (a) shows the nine clusters obtained from the NIRSpec light curves. The celerite fit for each light curve that comprises each cluster is shown in gray, and the average for each cluster is shown in the colored marker. The gray vertical lines in panel (a) of both Figures 5 and 6 mark the 2.4 hr rotation period of this object. Panel (b) shows the Sonora Diamondback contribution function for a clear atmosphere with $T_{\rm eff} = 1100$ K and $\log(g) = 4.5$. The colors are the same for the same clusters across both subplots. The clusters are overlaid onto the contribution function by calculating the average pressure of maximum flux for the wavelengths that comprise each cluster. The error bars on the clusters in panel (b) are the variance for the pressure of each cluster. The green shaded region represents the pressures where forsterite clouds exist, and the pink shaded region represents the pressures where iron clouds might exist from J. M. Vos et al. (2023).

same number of light curves. After binning the spectra by 0.5 μm and making the same SNR cuts as NIRSpec, the MIRI data result in 14 light curves. In each case, we allow the K-means clustering algorithm to determine the optimal number of clusters using the `KneeLocator` from `kneed` (V. Satopaa et al. 2011). `KneeLocator` applies the elbow method, which uses the sum of square errors to identify the point at which an additional cluster provides diminishing return. For NIRSpec, we allow the clustering algorithm to select between 1 and 80 clusters and for MIRI between 1 and 10 (compare to B. A. Biller et al. 2024, who allowed $n_{\rm cluster}$ to vary between 1 and 11 for both NIRSpec and MIRI). This difference in number of allowable clusters between NIRSpec and MIRI is due to the binning of the MIRI data, which resulted in only 14 light curves. The K-means clustering algorithm determines that the optimal number of clusters is 9 for NIRSpec and 2 for MIRI. This is an intriguing difference from B. A. Biller et al. (2024), who found 3 clusters for NIRSpec and 2 for MIRI for both components of the binary, despite both components having a similar effective temperature to SIMP 0136+0933.

At a first glance, we recognize that NIRSpec clusters 1–5, 6 and 7, and 8 and 9 appear similar (Figure 5). In addition to the

clustering algorithm identifying these clusters as distinct, we validated their uniqueness by conducting cosine similarity and Pearson correlation coefficient tests. We discuss the more nuanced differences between clusters, and what may cause them in, Sections 4.3 and 4.4.

4.3. Pressure Probed by Light-curve Clusters Can Inform the Primary Mechanism of Variability

The clustering algorithm reveals which wavelengths have similarly shaped light curves. Since physical mechanisms like clouds, aurora, hot spots, or chemical instabilities may all cause light-curve variability, we infer that similar shapes indicate shared physical mechanism(s). Panel (a) of Figures 5 and 6 show the clustered light curves, with gray vertical lines marking the object's 2.4 hr rotation period. The line in Figure 5 panel (a) is at 1 hr and in Figure 6 panel (a) at 3.4 and 5.8 hr.

We pair the multiwavelength clustering information with atmospheric models to provide insights into the atmosphere's vertical structure. Using the Sonora Diamondback models (C. V. Morley et al. 2024), we match each wavelength to its pressure/temperature layer. Figures 5 and 6 panel (b)
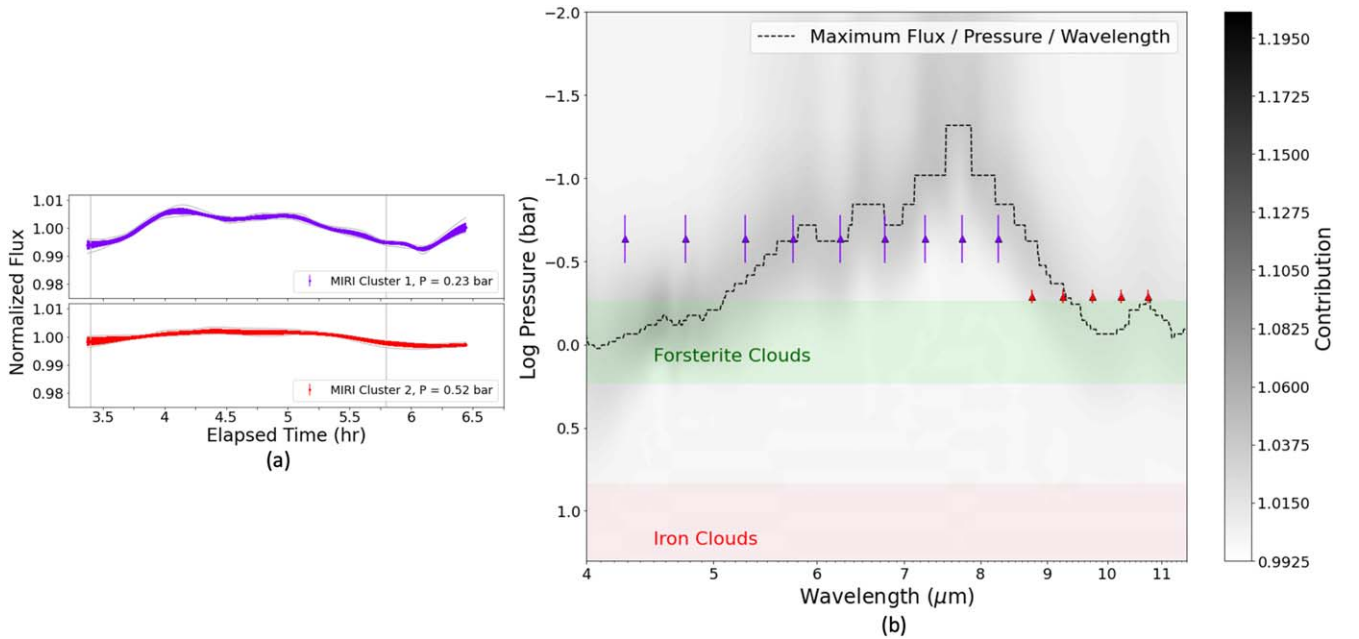
Figure 6. Panel (a) shows the two clusters obtained from the MIRI light curves. The celerite fit for each light curve that comprises each cluster is shown in gray, and the average for each cluster is shown in the colored marker. The gray vertical lines in panel (a) of both Figures 5 and 6 mark the 2.4 hr rotation period of this object. Panel (b) shows the Sonora Diamondback contribution function for a clear atmosphere with $T_{eff} = 1100$ K and $\log(g) = 4.5$. The colors are the same for the same clusters across both subplots. The clusters are overlaid onto the contribution function by calculating the average pressure of maximum flux for the wavelengths that comprise each cluster. The error bars on the clusters in panel (b) are the variance for the pressure of each cluster. The green shaded region represents the pressures where forsterite clouds exist, and the pink shaded region represents the pressures where iron clouds might exist from J. M. Vos et al. (2023).

overlay the NIRSpec and MIRI clusters on a clear-atmosphere contribution function at $T_{eff} = 1100$ K and $\log(g) = 4.5$ (similar to SIMP 0136+0933; J. Gagné et al. 2017; J. M. Vos et al. 2023). We use a cloudless contribution function because a clear atmosphere shows the deepest observable level in the atmosphere. The addition of inhomogeneous features would alter this function only to reveal shallower depths, not deeper. For instance, clouds flatten the contribution function at their formation pressure (see Figure 5 in J. M. Vos et al. 2023). We determine the average pressure probed for each cluster by determining the pressure that has the maximum flux contribution emitted by each wavelength in the cluster. This is shown in Figures 5 and 6 with error bars showing the pressure variance.

Prior works suggest physical mechanisms that may be responsible for SIMP 0136+0933's variability. A retrieval analysis by J. M. Vos et al. (2023) finds forsterite clouds at 0.55–1.7 bar and an iron cloud layer that is optically thick at 7 bar, shown as green and pink shaded regions in panel (b) of Figures 5 and 6. The presence of an iron cloud at 7 bar would block flux from deeper pressures in the 0.88–1.32 μm wavelength range, which is matched by NIRSpec Cluster 9 (red markers). Likewise, a forsterite cloud at 0.55–1.7 bar would block flux from that region or below, with wavelengths 0.81–2.17 μm (NIRSpec clusters 7–9) reflecting variability from forsterite cloud inhomogeneity. The forsterite cloud spans 0.55–1.7 bar, with clouds becoming optically thick at different pressures per wavelength, impacting flux in NIRSpec cluster 6. MIRI cluster 2's wavelengths probe the very top of the forsterite cloud layer and as such show low-variability amplitudes compared to other clusters, which probe a majority or the entirety of the forsterite cloud layer.

While clouds can explain variability in NIRSpec clusters 7–9, they alone cannot account for the variability observed in clusters 1–6. Clusters 1–3 probe higher than silicate cloud levels, while clusters 4–6 only probe the very top of the forsterite cloud. Since models show no clouds at pressures shallower than 0.55 bar, additional sources are needed for NIRSpec clusters 1–6. While J. M. Vos et al. (2023) did not consider a hot spot, J. K. Faherty et al. (2024) suggests that an aurorally driven temperature inversion may drive methane emission in a Y dwarf atmosphere. Strong aurorae in SIMP 0136+0933 (M. M. Kao et al. 2016, 2018) suggest that an aurorally driven temperature inversion may be plausible in this case too. Beyond aurora, rapid dynamical mixing may give rise to hot spots (C. V. Morley et al. 2014), and deeper temperature perturbations may be transported to lower pressures via radiative heating (T. D. Robinson & M. S. Marley 2014b; P. Tremblin et al. 2020).

We compare to the model spectra of C. V. Morley et al. (2014) in Figure 7, which inject energy at 0.1 bar and could represent any heating mechanism. Further work is needed to link specific mechanisms, like auroral heating, to spectral changes. The C. V. Morley et al. (2014) spectra show that a hot spot impacts wavelengths 2.2–3.8 μm and 5.4–8.5 μm, corresponding to NIRSpec cluster 1 and portions of clusters 2–6, as well as MIRI cluster 1. Wavelengths with the highest flux ratios, 2.6 and 3.2 μm, align with the maximum observed deviations, discussed in Section 4.4.

Finally, our analysis shows that NIRSpec clusters 2–6 probe similar pressures (0.42–0.66 bar) despite different light-curve shapes. We suspect these shape differences arise from the abundance of specific molecules. Labels for CO, CO_2, CH_4, and H_2O (Figure 7, bottom panel; Section 4.4) show which wavelengths are impacted by each molecule. For instance, NIRSpec cluster 1 traces the methane band from 3.2 to 3.7 μm, as predicted by P. Tremblin et al. (2020). Clusters 2–6 are more challenging to assign due to overlapping cross sections.
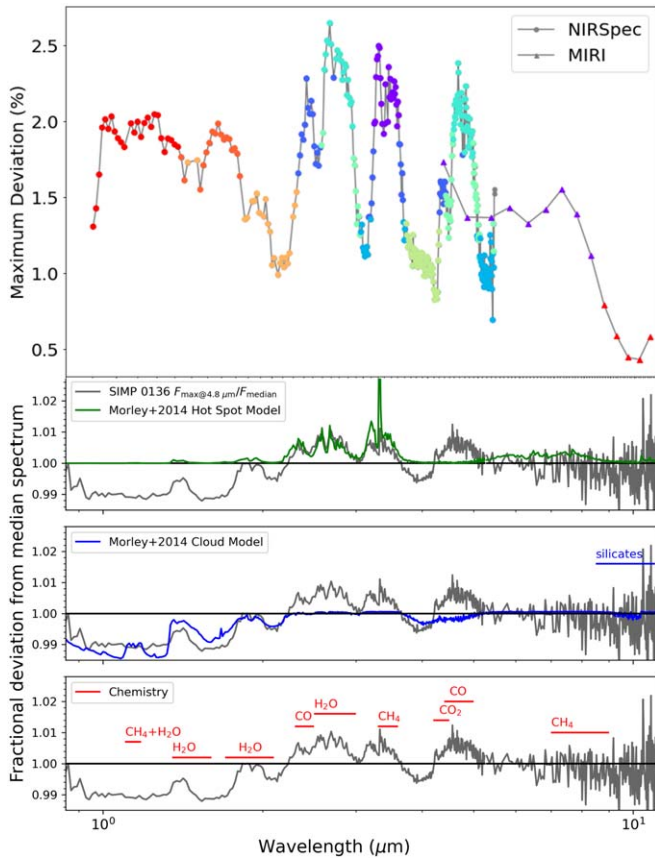
Figure 7. The top panel shows the measured maximum deviation of the light curves, colored by their respective cluster. The NIRSpec data are shown as circle markers and the MIRI data as triangles. The gray spectra in the three sub panels show the deviation of our "maximum" spectrum from our median spectra. The second panel shows the comparison between a scaled model flux ratio between a clear atmosphere and a clear atmosphere with a portion covered by a hot spot (C. V. Morley et al. 2014). The third panel highlights the flux ratio between a cloudy and clear atmosphere (C. V. Morley et al. 2014). The final panel labels the locations of impact for abundant molecules in the atmosphere.

It is likely that each cluster is impacted by a combination of mechanisms but at varying ratios. For this reason, we cannot rule out degeneracies in the combination of multiple mechanisms. For example, two clusters may probe pressures that are impacted by both clouds and a hot spot, but in one cluster, the clouds are the primary mechanism, and in another cluster, the hot spot is the primary mechanism, although the clouds still impact the light curve. The difference in primary mechanism is due to wavelengths affected by each mechanism (Figure 7).

4.4. Maximum Deviation as a Function of Wavelength

The top panel of Figure 7 shows the maximum observed flux deviation as a function of wavelength. Given the nonsinusoidal nature of these light curves, we define maximum flux deviation as the difference between the maximum and minimum normalized flux values of the celerite maximum likelihood fits. Notably, every wavelength displays variability. The maximum deviations occur near ~2.6 and ~3.2 μm. According to the contribution function in Figure 5, these wavelengths probe some of the highest altitudes in SIMP 0136+0933 and align with those most affected by an upper-atmosphere hot spot, as shown in the second panel of Figure 7. We do not carry out a full spectral modeling analysis in this Letter but simply

highlight the similarities between the observations and the predictions from C. V. Morley et al. (2014). Future atmospheric retrievals will better answer these questions.

Between ~5.5 and ~8.5 μm, we observe larger amplitudes than at wavelengths beyond ~8.5 μm, consistent with predictions from the C. V. Morley et al. (2014) hot spot model. These amplitude patterns support the presence of a hot spot in the upper atmosphere.

The second subpanel of Figure 7 shows flux ratio predictions driven by patchy clouds from C. V. Morley et al. (2014); ~1 to ~2.2 and ~3.7 to ~5 show a decreased flux due to the presence of clouds. These wavelengths roughly correspond to NIRSpec clusters 6–9, which all display a similar double trough shape.

A secondary amplitude peak appears at ~4.6 μm, not explained by the C. V. Morley et al. (2014) hot spot or cloud models. However, this peak aligns with the carbon dioxide bandpass (4.2–5.0 μm) and the carbon monoxide bandpass (4.4–5.2 μm), as shown in the bottom panel of Figure 7. Notably, NIRSpec clusters 1–5 (spanning ~2.2–3.7 μm and ~4.2–5.2 μm) all show a distinct trough near ~1.05 hr, suggesting a shared underlying mechanism for this feature. Since hot spot activity may drive variability from ~2.2 to ~3.7 μm, we infer that it may influence variability from ~4.2 to ~5.2 μm. Any disequilibrium species in the upper atmosphere would also vary in phase with the hot spot because the added energy from the hot spot could facilitate chemical interactions. In-depth atmospheric modeling, including both a hot spot model and disequilibrium chemistry, will be necessary to assess the impact of the hot spot on carbon chemistry within the atmosphere.

At a glance, NIRSpec clusters 1–5 have similar shapes due to a prominent trough near ~1 hr. However, detailed inspection shows significant differences in light-curve shapes beyond 2 hr, likely due to varying contributions from abundant molecules such as methane, water, carbon monoxide, and carbon dioxide (see J. J. Fortney et al. 2020). The impact of changing carbon chemistry is still an open question in the field, and further global circulation modeling efforts with disequilibrium chemistry will be needed to understand the scope of this variability mechanism (E. K. H. Lee et al. 2023, 2024).

Finally, MIRI cluster 2 (8.5–11 μm), shows less than 1% amplitude variability. While these wavelengths correspond to the silicate absorption region, the expected variability is low compared to the J band (Figure 7; J. M. Vos et al. 2023). However, J. L. Luna & C. V. Morley (2021) predict that wavelengths beyond 9 μm could exhibit enhanced variability due to patchy, high-altitude silicate clouds with small grains. In our analysis, we attribute increased variability from 5 to 8.5 μm to the hot spot presence. Similar reduced variability beyond 8.5 μm is observed by B. A. Biller et al. (2024) for WISE1049AB, likely due to silicate absorption properties, which are prominent from L4 to L6 but absent by L8 (G. Suárez & S. Metchev 2022). In T dwarfs, forsterite clouds form deeper in the atmosphere than in their warmer L dwarf counterparts. In this case, the wavelengths that make up MIRI cluster 2 probe the very top of the forsterite cloud layer, and as such any inhomogeneity in the cloud layer has minimal impact in the variations in brightness.

4.5. Comparison with Previous Studies

SIMP 0136 has been extensively studied using a range of observational and analysis techniques. D. Apai et al. (2013)

obtained HST/WFC3 spectroscopic monitoring of SIMP 0136 +0933, reporting a 4.5% amplitude, higher than our maximum flux deviation across all wavelengths. They also observed significant light-curve evolution. H. Yang et al. (2016) conducted simultaneous Spitzer and HST observations, finding wavelength-dependent differences in light-curve shape and amplitude, consistent with our results. In their study, the *J* band light curve had an amplitude of ~5%, greater than our ~2% maximum deviation, while Spitzer showed ~1% amplitude, lower than our observed deviations (Figure 7; H. Yang et al. 2016). They reported a ~30° phase shift between HST *J* band and Spitzer channel one but found no phase shift in and out of the water bands. They attributed different light-curve shapes to wavelengths probing opposite sides of ~4 bar, near the radiative–convective boundary. A. M. McCarthy et al. (2024) identified a ~40° phase shift between *J* band and *K* band, linking it to multiple patchy cloud layers. Similarly, M. K. Plummer et al. (2024) reported a ~90° phase shift between *H*–*K* and *J*–*H* light curves, suggesting complex vertical structure and wave-induced cloud breakup in SIMP 0136's atmosphere.

Previous studies (e.g., E. Buenzli et al. 2012; B. A. Biller et al. 2013; H. Yang et al. 2016; B. W. P. Lew et al. 2020; A. M. McCarthy et al. 2024) have noted phase shifts between light curves in different photometric bands for many brown dwarfs and planetary-mass objects, including SIMP 0136. However, our results indicate that rather than a true phase shift, distinct light-curve shapes arise from different variability mechanisms present at varying depths (pressure/temperature levels). Broadband photometric observations may capture multiple mechanisms, creating the illusion of a phase shift in the integrated light curve arising from the superposition of multiple variability mechanisms. Since JWST provides both extensive wavelength range with adequate resolution, we can discern these distinct light-curve shapes, allowing us to uncover the drivers of variability.

5. Summary and Conclusions

This study, the first JWST spectroscopic variability analysis of a planetary-mass object, demonstrates JWST's unique power to probe extrasolar atmospheres. As a young exoplanet analog, SIMP 0136+0933 is an ideal laboratory for studying the diversity of atmospheric variability mechanisms from 1 to 12 μm. The results highlight the potential of combining advanced atmospheric models with JWST spectroscopic observations and motivate further JWST variability studies of extrasolar atmospheres.

We report spectroscopic monitoring results from ~3 hr of NIRSpec/BOTS followed by ~3 hr of MIRI/LRS of the planetary-mass object SIMP 0136+0933 (rotation period 2.4 hr). Variability is seen at all wavelengths, with the largest maximum flux deviation of 2.6% at 2.6 μm. The light-curve structure changes across wavelength and pressure, indicating multiple atmospheric variability mechanisms.

Atmospheric features like clouds, aurora, hot spots, a reduced temperature gradient, or changing carbon chemistry could impact flux at specific wavelengths. Grouping light curves by shape, we identify which wavelengths are impacted by the same mechanism(s). We find nine clusters in NIRSpec and two in MIRI, linked to patchy clouds, hot spots, and varying carbon chemistry.

Previous studies (D. Apai et al. 2013; J. M. Vos et al. 2023) suggest cloud layers at ~1 and ~7 bar, impacting wavelengths from 0.88 to 2.17 μm, corresponding to NIRSpec clusters 7, 8, and 9. Wavelengths beyond ~2.2 μm correspond to NIRSpec clusters 1–6, showing broadly similar light-curve shapes but different substructure beyond 2 hr. A hot spot, possibly from aurora (M. M. Kao et al. 2016, 2018), rising/falling air pockets (C. V. Morley et al. 2014), or deeper temperature perturbations (T. D. Robinson & M. S. Marley 2014b), likely affects wavelengths ~2.2–3.7 μm (Figure 4 in C. V. Morley et al. 2014). These correspond to NIRSpec cluster 1 and parts of clusters 2–6. Furthermore, changes in methane, water, carbon monoxide, and carbon dioxide likely cause variability, which then causes impacted wavelengths' light curves to differentiate into distinct clusters.

The two MIRI clusters are split at ~8.5 μm, coinciding with the end of hot spot–driven variations (~5.5–8.5 μm; Figure 4 in C. V. Morley et al. 2014) and the onset of the silicate absorption feature (G. Suárez & S. Metchev 2022), suggesting sensitivity to these mechanisms.

However, this is just a glimpse into SIMP 0136+0933's atmosphere. Like planets in our solar system, its atmosphere exhibits long-term changes (H. Yang et al. 2016; B. Croll et al. 2016). Longer observations spanning multiple rotations are crucial for deeper insights into evolving atmospheric mechanisms and distinguishing variability timescales. Monitoring changes in light-curve shapes over time will help disentangle these mechanisms and assess their correlations.

This is the first Letter in a series exploring the data from Section 2. Detailed modeling, retrievals, and spectral analysis will follow, offering a deeper understanding of the physical drivers of variability on this extrasolar world.

All JWST data used in this Letter can be found in MAST: 10.17909/pfnd-md36

Facility: JWST

Software: Astropy (Astropy Collaboration et al. 2022), SciPy (P. Virtanen et al. 2020), celerite2 (D. Foreman-Mackey 2018), emcee (D. Foreman-Mackey et al. 2013b)

ORCID iDs

Allison M. McCarthy ⓘ https://orcid.org/0000-0003-2015-5029
Johanna M. Vos ⓘ https://orcid.org/0000-0003-0489-1528
Philip S. Muirhead ⓘ https://orcid.org/0000-0002-0638-8822
Beth A. Biller ⓘ https://orcid.org/0000-0003-4614-7035
Caroline V. Morley ⓘ https://orcid.org/0000-0002-4404-0456
Jacqueline Faherty ⓘ https://orcid.org/0000-0001-6251-0573
Ben Burningham ⓘ https://orcid.org/0000-0003-4600-5627
Emily Calamari ⓘ https://orcid.org/0000-0002-2682-0790
Nicolas B. Cowan ⓘ https://orcid.org/0000-0001-6129-5699
Kelle L. Cruz ⓘ https://orcid.org/0000-0002-1821-0650
Eileen Gonzales ⓘ https://orcid.org/0000-0003-4636-6676
Mary Anne Limbach ⓘ https://orcid.org/0000-0002-9521-9798
Pengyu Liu ⓘ https://orcid.org/0000-0001-7047-0874
Evert Nasedkin ⓘ https://orcid.org/0000-0002-9792-3121
Genaro Suárez ⓘ https://orcid.org/0000-0002-2011-4924
Xianyu Tan ⓘ https://orcid.org/0000-0003-2278-6932
Cian O'Toole ⓘ https://orcid.org/0000-0002-1699-2222
Channon Visscher ⓘ https://orcid.org/0000-0001-6627-6067
Niall Whiteford ⓘ https://orcid.org/0000-0001-8818-1544
Yifan Zhou ⓘ https://orcid.org/0000-0003-2969-6040

References

Ahrer, E.-M., Stevenson, K. B., Mansfield, M., et al. 2023, Natur, 614, 653
Alderson, L., Wakeford, H. R., Alam, M. K., et al. 2023, Natur, 614, 664
Apai, D., Radigan, J., Buenzli, E., et al. 2013, ApJ, 768, 121
Artigau, É., Bouchard, S., Doyon, R., & Lafrenière, D. 2009, ApJ, 701, 1534
Artigau, É., Doyon, R., Lafrenière, D., et al. 2006, ApJL, 651, L57
Astropy Collaboration, Price-Whelan, A. M., Lim, P. L., et al. 2022, ApJ, 935, 167
Beiler, S. A., Mukherjee, S., Cushing, M. C., et al. 2024, ApJ, 973, 60
Biller, B. A., Crossfield, I. J. M., Mancini, L., et al. 2013, ApJL, 778, L10
Biller, B. A., Vos, J. M., Zhou, Y., et al. 2024, MNRAS, 532, 2207
Buenzli, E., Apai, D., Morley, C. V., et al. 2012, ApJL, 760, L31
Croll, B., Muirhead, P. S., Lichtman, J., et al. 2016, arXiv:1609.03587
Faherty, J. K., Riedel, A. R., Cruz, K. L., et al. 2016, ApJS, 225, 10
Faherty, J. K., Burningham, B., Gagné, J., et al. 2024, Natur, 628, 511
Foreman-Mackey, D. 2018, RNAAS, 2, 31
Foreman-Mackey, D., Agol, E., Ambikasaran, S., & Angus, R. 2017, AJ, 154, 220
Foreman-Mackey, D., Hogg, D. W., Lang, D., & Goodman, J. 2013a, PASP, 125, 306
Foreman-Mackey, D., Hogg, D. W., Lang, D., & Goodman, J. 2013b, PASP, 125, 306
Fortney, J. J., Visscher, C., Marley, M. S., et al. 2020, AJ, 160, 288
Gagné, J., Faherty, J. K., Burgasser, A. J., et al. 2017, ApJL, 841, L1
Hallinan, G., Littlefair, S. P., Cotter, G., et al. 2015, Natur, 523, 568
Jakobsen, P., Ferruit, P., Alves de Oliveira, C., et al. 2022, A&A, 661, A80
Kao, M. M., Hallinan, G., Pineda, J. S., et al. 2016, ApJ, 818, 24
Kao, M. M., Hallinan, G., Pineda, J. S., Stevenson, D., & Burgasser, A. 2018, ApJS, 237, 25
Kühnle, H., Patapis, P., Mollière, P., et al. 2024, arXiv:2410.10933
Lee, E. K. H., Tan, X., & Tsai, S.-M. 2023, MNRAS, 523, 4477
Lee, E. K. H., Tan, X., & Tsai, S.-M. 2024, MNRAS, 529, 2686
Lew, B. W. P., Apai, D., Zhou, Y., et al. 2020, AJ, 159, 125
Liu, P., Biller, B. A., Vos, J. M., et al. 2024, MNRAS, 527, 6624
Luna, J. L., & Morley, C. V. 2021, ApJ, 920, 146
McCarthy, A. M., Muirhead, P. S., Tamburo, P., et al. 2024, ApJ, 965, 83
Metchev, S. A., Heinze, A., Apai, D., et al. 2015, ApJ, 799, 154
Morley, C. V., Marley, M. S., Fortney, J. J., & Lupu, R. 2014, ApJL, 789, L14
Morley, C. V., Mukherjee, S., Marley, M. S., et al. 2024, ApJ, 975, 59
Plummer, M. K., Wang, J., Artigau, É., Doyon, R., & Suárez, G. 2024, ApJ, 970, 62
Radigan, J. 2014, ApJ, 797, 120
Rasmussen, C. E., & Williams, C. K. I. 2006, Gaussian Processes for Machine Learning (Cambridge, MA: MIT Press),
Robinson, T. D., & Marley, M. S. 2014a, ApJ, 785, 158
Robinson, T. D., & Marley, M. S. 2014b, ApJ, 785, 158
Rustamkulov, Z. & Transiting Exoplanet Community ERS Team 2022, BAAS, 54, 102.218
Satopaa, V., Albrecht, J., Irwin, D., & Raghavan, B. 2011, in 2011 31st Int. Conf. on Distributed Computing Systems Workshops (Piscataway, NJ: IEEE), 166
Sing, D. K., Evans-Soma, T. M., Rustamkulov, Z., et al. 2024, AJ, 168, 231
Suárez, G., & Metchev, S. 2022, MNRAS, 513, 5701
Tan, X., & Showman, A. P. 2021, MNRAS, 502, 678
Tremblin, P., Amundsen, D. S., Chabrier, G., et al. 2016, ApJL, 817, L19
Tremblin, P., Phillips, M. W., Emery, A., et al. 2020, A&A, 643, A23
Virtanen, P., Gommers, R., Oliphant, T. E., et al. 2020, NatMe, 17, 261
Vos, J. M., Faherty, J. K., Gagné, J., et al. 2022, ApJ, 924, 68
Vos, J. M., Burningham, B., Faherty, J. K., et al. 2023, ApJ, 944, 138
Welbanks, L., Line, M., Carter, A., et al. 2024, AAS/Division for Extreme Solar Systems Abstracts, 56, 201.02
Yang, H., Apai, D., Marley, M. S., et al. 2016, ApJ, 826, 8
Zhang, X., & Showman, A. P. 2014, ApJL, 788, L6